



## Flame-based processing as a practical approach for manufacturing hydrogen evolution electrodes



Justin Roller <sup>a,b,\*</sup>, Julie Renner <sup>c</sup>, Haoran Yu <sup>a,d</sup>, Chris Capuano <sup>c</sup>, Tony Kwak <sup>a,b</sup>, Yang Wang <sup>a,b</sup>, C. Barry Carter <sup>a,d</sup>, Kathy Ayers <sup>c</sup>, William E. Mustain <sup>b,d</sup>, Radenka Maric <sup>a,b,d</sup>

<sup>a</sup> Department of Materials Science and Engineering, University of Connecticut, 191 Auditorium Rd., Storrs, CT 06269, USA

<sup>b</sup> Center for Clean Energy Engineering, University of Connecticut, 44 Weaver Rd., Storrs, CT 06269, USA

<sup>c</sup> Proton OnSite, 10 Technology Drive, Wallingford, CT 06492, USA

<sup>d</sup> Department of Chemical & Biomolecular Engineering, University of Connecticut, Storrs, CT 06269, USA

### HIGHLIGHTS

- A deposition study is employed using RSDT to deposit catalysts in one step.
- All combinations of catalyst with Nafion® as the binder remained intact after polarization.
- Processing conditions can result in either amorphous or crystalline Pt.
- Deposition of Pt/Vulcan XC-72R onto Toray paper resulted in the best performance.
- The RSDT GDE configuration operated at 70% efficiency with a 5× reduction in Pt.

### ARTICLE INFO

#### Article history:

Received 30 April 2014

Received in revised form

1 August 2014

Accepted 3 August 2014

Available online 10 August 2014

#### Keywords:

Hydrogen evolution  
Reactive spray deposition  
Electrolysis  
Catalysts  
Electrode development

### ABSTRACT

Catalyst structure and morphology are inevitably dictated by the synthesis route, which in-turn dictates catalyst activity, stability and utilization in the electrode. Reactive spray deposition technology (RSDT) is a promising synthesis route for electrode manufacturing because of the potential to achieve high-throughput processing under a diverse range of process configurations. This work investigates several unique approaches to Pt catalyst deposition using jet-flame synthesis for water electrolysis electrodes. Direct application of the catalyst film onto Nafion 117 and carbon paper is explored along with approaches to dispersing the Pt onto carbon or  $Ti_nO_{2n-1}$ . Operational challenges relating to the harsh conditions of  $H_2$  evolution and electrode adhesion are addressed by adding binder and catalyst support to the electrode structure. The RSDT technology produces an electrode, coated directly onto Nafion 117®, with a 20-fold reduction in Pt loading while maintaining high in-cell performance (2.1 V at 2 A cm<sup>-2</sup>) compared to an industry-level baseline. Durability testing at 1.8 A cm<sup>-2</sup>, 400 psi differential pressure and a temperature of 50 °C yields a consistent potential of ~2.2 V for over 1100 h without failure. The same electrode applied directly to carbon paper resulted in a voltage of ~2.1 V for ~600 h without failure.

© 2014 Elsevier B.V. All rights reserved.

## 1. Introduction

### 1.1. Hydrogen

Hydrogen is a widely used industrial gas, with a large and expanding global market. Over 10 million metric tons of hydrogen are produced in the US each year [1]. High-purity hydrogen is used in a variety of applications including fuel cell operation, electric generator cooling, chemical production, heat treating, semiconductor processing, and as a laboratory carrier or fuel gas. Hydrogen also has the potential to become a significant alternative

\* Corresponding author. Department of Materials Science and Engineering, University of Connecticut, 191 Auditorium Rd., Unit 3222, Storrs, CT 06269, USA.

E-mail addresses: [Justin.roller@engr.uconn.edu](mailto:Justin.roller@engr.uconn.edu), [justin.roller@fei.com](mailto:justin.roller@fei.com) (J. Roller), [jrenner@protononsite.com](mailto:jrenner@protononsite.com) (J. Renner), [haoran.yu@uconn.edu](mailto:haoran.yu@uconn.edu) (H. Yu), [ccapuano@protononsite.com](mailto:ccapuano@protononsite.com) (C. Capuano), [dongwook.kwak@uconn.edu](mailto:dongwook.kwak@uconn.edu) (T. Kwak), [yang.2.wang@uconn.edu](mailto:yang.2.wang@uconn.edu) (Y. Wang), [cbarter@engr.uconn.edu](mailto:cbarter@engr.uconn.edu) (C.B. Carter), [kayers@protononsite.com](mailto:kayers@protononsite.com) (K. Ayers), [maric@engr.uconn.edu](mailto:maric@engr.uconn.edu) (R. Maric).

fuel because it offers a range of potential benefits including increased energy security, reduced dependence on foreign oil, and reduced greenhouse gas emissions. As a potential energy storage carrier, hydrogen can serve as a link between electric and gas infrastructures and provide ancillary services to the grid such as frequency regulation and load shifting.

### 1.2. Membrane-based electrolysis

Proton exchange membrane (PEM)-based systems have many advantages over other hydrogen production technologies. Compared to hydrocarbon steam reforming, PEM technology is more environmentally friendly, especially when combined with a renewable energy source, and easily scales down, enabling efficient, cost-effective on-site production and reduces the need to ship hydrogen from a centralized location. In addition, membrane-based electrolysis produces very pure hydrogen, with none of the typical catalyst poisons that are found in hydrogen produced from reforming. PEM-based systems do not require corrosive electrolytes such as those used in the liquid potassium hydroxide (KOH) electrolyte-based systems. In addition, PEM-based systems have a more compact footprint, and the ability to generate hydrogen at high pressure while operating at ambient oxygen pressure, which increases safety and reduces cost compared to KOH-based systems.

For energy storage applications, PEM electrolysis has been selected as the technology of choice [2]. The cell stacks respond quickly and robustly to variable input load, thus enabling a variety of energy capture applications. Siemens has recently announced that their product development will focus on PEM electrolysis, and even companies with established KOH-based products are investigating PEM technology for energy applications [4]. While PEM-based systems have many advantages, significant development in materials and manufacturing are needed for large-scale energy applications.

For example, most commercial electrolyzers use unsupported catalysts and manual electrode fabrication and testing processes. This results in high noble metal loadings and high labor costs to manufacture the membrane electrode assembly (MEA), which accounts for nearly one-fifth of the total stack cost. As the development of larger scale electrolysis for energy applications becomes closer to reality, higher MEA manufacturing speed, lower manufacturing energy, and lower catalyst loadings are essential for market success.

### 1.3. Ultra-low loading

Conventional electrode fabrication processes involve multiple manual steps such as mixing of catalyst and binder materials, inking, sintering, and decal transfer in a high temperature press. Reduction in the thickness of the electrode layer (and consequently reduction in catalyst loading), while still achieving acceptable uniformity, is challenging in the current process.

Electrolysis electrodes have to withstand different operating conditions than fuel cell electrodes, such as significantly higher potential on the oxygen electrode, full humidification with high water uptake, and high mechanical stress due to gas evolution at high current densities, resulting in large amounts of bubble formation at the electrode surface. Alternate fabrication processes that provide tunable control over electrode structure, such as spraying [5,6], sputtering [7], nano-structured thin-films [8], and flame spray pyrolysis [9–11] are, therefore, key areas for development.

### 1.4. RSDT

RSDT is a variant of flame spray pyrolysis (FSP) [12] and spray pyrolysis (SP) [13]. The RSDT approach uses the combustion

enthalpy of a solvent to decompose the precursor in the turbulent confines of a jet-flame. Catalyst production and electrode formation are combined into one step, which takes place in the open atmosphere and eliminates the need to dispose of solvent waste; the solvent is completely combusted to CO<sub>2</sub> and H<sub>2</sub>O. A wide array of material systems have been made using RSDT including Pt, CeO<sub>2</sub>, SnO<sub>2</sub>, Sn–Pt, LiCoO<sub>2</sub>, Ir<sub>x</sub>Pt<sub>1-x</sub>O<sub>2-y</sub>, Ir<sub>x</sub>Ru<sub>1-x</sub>O<sub>2-y</sub> and Gd<sub>0.2</sub>Ce<sub>0.8</sub>O<sub>1.9</sub> [10,11,14–21].

Nucleation of the metal occurs from the vapor phase, along with growth of the primary particle throughout the length of the hot reactive zone [22] as shown in Fig. 1. Formation of the nanocrystallite particles, during time-of-flight, occurs prior to film formation through a multi-step process on a time scale of milliseconds. The general mechanism of particle growth, once the precursor has vaporized, occurs by: homogeneous reactions, nucleation, surface growth, cluster formation (a transitory state between single atoms and solid material), coalescence, aggregation, and agglomeration [23–26]. Depending on the processing conditions, a film can form either from the vapor phase (*i.e.*, direct impingement of the flame onto the substrate), by a physical impingement (ballistic deposition) of a fully formed nanoparticle, or by a combination of both mechanisms. The exact growth mechanism is affected by the synthesis thermal profile, concentration of reactants, the precursor composition, oxidant/fuel flow rates, and residence time. In co-flow atomizing-burners, the oxidant and fuel flow rates, combined with the exit orifice geometries, strongly affect the mixing [27–29]. The mixing determines residence time and temperature profile of the flame.

Primary particle growth can be arrested through rapid cooling by an air quench (labeled ‘quench point’ and denoted as a vertical line in Fig. 1), to create a fast non-equilibrium phase change [30]. Stand-off distance, temperature and location(s) of the quench are also critical to the formation of the desired metal and morphology [25]. The quench has two distinct functions: it stops particle growth, and it allows a wider range of substrate materials to be positioned at lower stand-off distances. This is crucial for direct deposition onto polymeric electrolytes such as Nafion® which has a glass transition point at 110 °C [31]. While passing through the quench, the temperature drops 200–400 °C cm<sup>-1</sup> and the luminosity of the flame is greatly diminished. The post-quench product stream consists of nanoparticles that can enter into an optional secondary spray zone where two air-assist atomizers inject a suspended support material into the cooled reactant gas stream. The droplets are entrained and mixed with the process stream prior to striking the substrate.

In this work, RSDT was used to prepare new high performance electrode structures for hydrogen evolution in PEM-based water electrolysis. Specifically, this study investigated the deposition of hydrogen evolution catalysts under varying quench temperatures and flow rates. The prepared electrodes were characterized by transmission electron microscopy (TEM), X-ray diffraction (XRD) and scanning electron microscopy (SEM). Electrode and cell configuration adjustments, and variable cell testing conditions were used to understand the most important parameters and guide development.

## 2. Experimental

### 2.1. Chemicals and materials

Pt acetylacetone (Pt(acac)<sub>2</sub>, Colonial Metals, Elkton, MD) was used as the Pt source. Pt(acac)<sub>2</sub>, is one of the most highly available and least expensive organoplatinum compounds, and is widely used in catalysis [32,33]. Additionally it is free of potential halide or

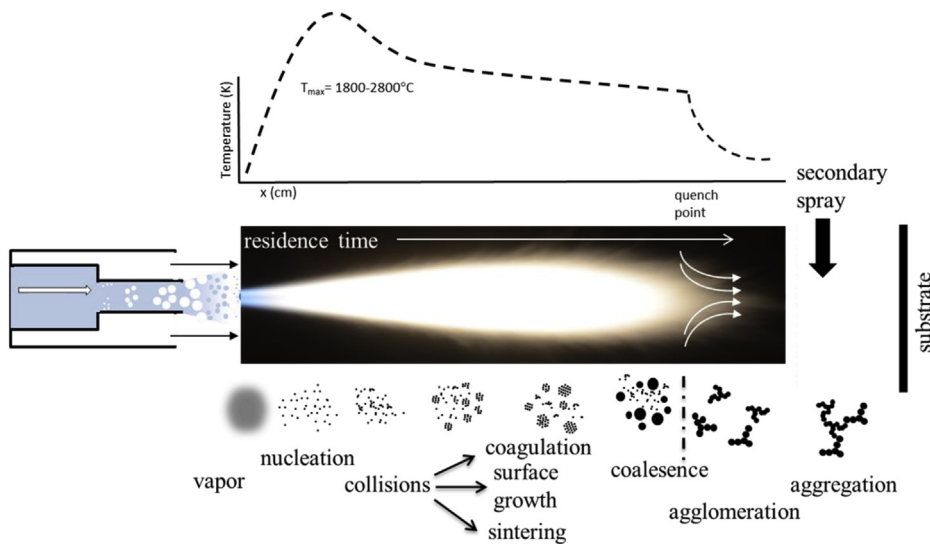


**Fig. 1.** The RSDT spraying and combustion process involves the evolution and growth of particles from a supersaturated vapor in the flame and the development of a temperature profile. The growth mechanism of the particles can be controlled by changing the thermal profile, concentration of reactants, precursor composition, oxidant/fuel flow rates, and residence time.

nitrate contaminants [34]. Xylene, acetone (ACS reagent grade, Sigma Aldrich, St. Louis MO) and thiol-free propane (Airgas East Inc., Cheshire CT) were used as the solvents.

For supported Pt depositions, dispersions were made using methanol. The carbon support used in this work was Vulcan XC-72R (Cabot, Boston, MA) and the titanium sub-oxide support (*i.e.*, Magneli phases) of the general formula  $\text{Ti}_n\text{O}_{2n-1}$  was Ebonex® (10015, Atraverda Ltd., Gwent, UK). The binder/ionomer (Nafion® 117 solution, Sigma Aldrich, St. Louis MO) was a 5 wt.% dispersion in a mixture of lower aliphatic alcohols and water. The commercial Ebonex® material was ball milled for 100 h before use to reduce the particle size [10]. A slurry of  $\text{Ti}_n\text{O}_{2n-1}$  was prepared by mixing a 50/50 vol.% deionized water/methanol solution with Nafion® ionomer. Substrates submitted for electrolyzer testing were deposited as ½ MEAs. Two types of substrates were used for direct coating by the RSDT process followed by electrolysis testing. One substrate was Nafion 117® (178  $\mu\text{m}$  thick) a chemically stabilized perfluorosulfonic acid/polytetrafluoroethylene copolymer in the acid ( $\text{H}^+$ ) form (DuPont, Wilmington, DE). The other substrate was TGP-H-120 Toray carbon paper.

## 2.2. RSDT

The electrocatalyst electrode layers were synthesized in a one-step process using RSDT [10,14,21,35]. Pt films were deposited onto either a  $25\text{ cm}^2$  (square format) or  $28\text{ cm}^2$  (circle format) substrate. To aid in atomization, and to increase the heat released in the combustion zone liquid propane was added to a 1 L closed vessel of the precursor solution. Precursor solution was continuously passed through the RSDT atomizing-burner at a constant flow rate of  $4\text{ mL min}^{-1}$  and the precursor was heated to approximately  $60^{\circ}\text{C}$  by setting the atomizing-burner to  $190^{\circ}\text{C}$  in all experiments. The exit orifice was surrounded by a channel which passed  $\text{O}_2$  as the fuel oxidant at  $13.6\text{ L min}^{-1}$ . In order to bring the substrate closer to the process while maintaining the deposition temperature at  $\sim 120^{\circ}\text{C}$ , a quench gas of air, flow rate  $28.3-85\text{ L min}^{-1}$ , was used to rapidly cool the combustion zone at distances of 4–10 cm from the location of the spray injection. The distance between the burner face and the substrate was 18 cm.

Specific electrode formulations are described as follows. For selected cathode depositions, a catalyst support (*i.e.*, Vulcan XC-72R

or Ebonex®) was introduced into the process using two 781S-46F air-assist nozzles (EFD, Inc., East Providence, RI) mounted at  $180^{\circ}$  from each other and transverse to the centerline of the flame axis. The total flow rate of the slurry was set to  $0.75\text{ mL min}^{-1}$  per nozzle (total flow rate:  $1.5\text{ mL min}^{-1}$ ); the atomizing air was supplied to the nozzle's fan cap at  $68.9-82.7\text{ kPa}$ . Each slurry solution was prepared using methanol or methanol/water as the liquid phase. Once the support phase was added, the entire solution was sonicated (Misonix S-4000, QSonica, LLC, Newton CT) prior to filling the syringe pump.

Process conditions and specific formulations for depositions in this study are listed in Table 1. Unless noted all electrodes were fabricated by the catalyst coated membrane (CCM) approach whereby the catalyst is applied directly to the membrane.

## 2.3. Physical characterization

Bulk elemental analysis of the deposited films was determined by inductively coupled plasma optical emission spectroscopy (ICP-OES) using a Perkin Elmer Optima 7300DV ICP-OES. The structure of the deposited Pt was probed by a Bruker D8 Advance X-ray diffractometer configured with: a  $\varnothing 250\text{ mm}$  goniometer in Bragg–Brentano geometry; a  $\text{Cu K}_{\alpha}$  ( $1.541\text{ \AA}$ ) source; and a compound silicon strip 1-dimensional LynxEye detector.

SEM images were captured using a FEI Quanta 250 FEG with a field emission source and imaged using an Everhart–Thornley SE (secondary electron) detector with an electron accelerating voltage of 10 or 20 kV and a working distance of 10 mm. A series of electron micrographs were collected with a Tecnai T12 120 kV TEM. In addition, images were collected with an aberration-corrected (probe) FEI Titan G2 80-200 with ChemiSTEM. The Titan was equipped with a X-FEG high-brightness gun and a DCOR  $C_s$ -probe corrector. Z-contrast images were generated by high-angle annular dark field (HAADF) scanning transmission electron microscopy (STEM). By using a HAADF detector, electrons are collected which are not Bragg scattered therefore the HAADF images show little or no diffraction effects. Elemental maps were acquired using a ChemiSTEM windowless SDD for X-ray energy dispersive spectroscopy (XEDS). The TEM grids were placed at an equivalent stand-off distance to the electrodes and removed at timed intervals as noted.

**Table 1**

Processing conditions for electrodes applied by the RSDT method.

Sample	Substrate	Deposition time [min]	Quench distance [cm]	Substrate temperature [°C]	Catalyst	Binder	Quench (air) flow rate [L min <sup>-1</sup> ]	Loading [mg cm <sup>-2</sup> ]	Electrode thickness average [nm]
A-Pt-30	RDE	30	Short	110	Pt	None	Medium	0.03	NA
B-Pt-Ebonex-30	RDE	30	Short	106	Pt/Ti <sub>n</sub> O <sub>2n-1</sub>	None	Medium	0.03	NA
C-Pt-103	Nafion 117®	103	Short	120	Pt	None	High	0.1	170
D-Pt-230	Nafion 117®	229	Short	110	Pt	None	High	0.18	554
E-Pt-130	Nafion 117®	132	Long	140	Pt	None	Low	0.2	335
F-Pt-110	Nafion 117®	111	Short	91	Pt	None	Low	0.11	188
G-Pt-Ebonex-130	Nafion 117®	131	Short	114	Pt/Ti <sub>n</sub> O <sub>2n-1</sub>	3.37 wt.% I/E = 0.44	Medium–high	0.13	~3500
				128					
H-Pt-Vulcan-227	Nafion 117®	227	Short	128	Pt/Vulcan XC-72R	0.98 wt.% I/C = 0.15	Low	0.4	~7000
I-Pt-Nafion-118	Nafion 117®	118	Short	141	Pt/Nafion (ionomer)	0.98 wt.% no carbon	Low	0.1	250
J-Pt-Vulcan-224	Nafion 117® (28 cm <sup>2</sup> )	224	Long	111	Pt/Vulcan XC-72R	0.98 wt.% I/C = 0.15	Low	0.4	~7000
K-Pt-Vulcan 230	Toray (28 cm <sup>2</sup> )	230	Long	125.5	Pt/Vulcan XC-72R	0.98 wt.% I/C = 0.15	Low	0.4	~7000

## 2.4. Electrochemical measurements

Electrochemical measurements were performed in a three-electrode, single-compartment half-cell using a reversible hydrogen electrode (RHE) (ET071 Hydroflex, eDAQ) as the reference electrode. A Pt wire (0.5 mm OD × 152 mm L, 99.95%) in a fritted tube was used as the counter electrode (AFCTR5, Pine Instruments). The working electrode was formed by directly depositing the Pt or Pt/Ebonex onto a 5 mm hands-off glassy carbon disk assembly (ACE6DC050GC, Pine Instruments) and then tested for surface area by hydrogen adsorption/desorption, i.e.,  $H_{\text{ads}}/H_{\text{des}}$ . All potentials reported are relative to a RHE immersed in 0.1 M HClO<sub>4</sub> at 25 °C. Cyclic voltammetry (CV) was performed using a PGSTAT 302N potentiostat (Ecochemie), controlled with Nova software version 1.7. Rotating disc voltammetry was performed using an ASR rotator (AFMSRCE, Pine Instruments). The whole 125 mL half-cell (AKCELL3, Pine Instruments) was surrounded by a water jacketed sheath with the water temperature thermostated to 25 °C (Isotemp 3016D, Fisher).

## 2.5. Electrolyzer testing

Initial electrolyzer experiments to assess performance were conducted using modified 25 cm<sup>2</sup> fuel cell hardware (Fuel Cell Technologies, Inc., 25 SCH) at 50 °C. The graphite flow field on the oxygen evolution side was replaced with a titanium flow field for stability at high electrolysis potentials. ½ MEAs and GDEs (gas diffusion electrodes) were assembled into the test cell by placing the RSDT applied electrode (typically a ½ MEA) in contact with the appropriate baseline GDE on the other side of the membrane. The MEA was assembled using Teflon gaskets and the bolts were torqued to 40 in-lbs.

The electrolyzer was operated by circulating ultrapure water through the anode side of the cell. The polarization curves were recorded by step changes in the current density, up to 2000 mA cm<sup>-2</sup>. The current was held for several minutes at each step to allow the voltage to stabilize. The baseline configurations used for reference consisted of an MEA with IrO<sub>2</sub> as the oxygen evolution reaction (OER) catalyst and Pt, as the hydrogen evolution reaction (HER) catalyst, directly deposited on a N117 membrane, and an IrO<sub>2</sub> OER GDE and Pt HER GDE separated by a N117 membrane.

Durability/stability testing was conducted using Proton's laboratory product commercial hardware for the HyGen 200 series of gas generators, enabling differential hydrogen pressure operation on a 28 cm<sup>2</sup> stack.

## 3. Results and discussion

Two different approaches were taken to deposit the hydrogen evolution electrode onto N117. These approaches included unsupported Pt thin-films (<1 μm thick) and a supported Pt configuration (>3–8 μm thick). The thickness of the supported Pt electrodes was largely dictated by the support material. Both approaches were evaluated to determine the optimal configuration for electrolysis.

### 3.1. Unsupported Pt thin-film approach

Unsupported Pt electrodes were deposited directly onto a N117 membrane. Process parameters of deposition time (thickness), location of quench, and flow rate of the quench were explored. Also, the electrochemical performance for H<sub>2</sub> oxidation and reduction was examined. Deposition conditions used to produce the unsupported thin-film electrodes are listed in Table 1.

### 3.2. Control of film thickness and crystallinity using the RSDT process

Process parameters were initially optimized for the thin film approach. SEM images of example films are shown in Fig. 2. The thickness was 170 or 550 nm depending on the process time, 103 or 230 min, respectively.

A distinctive nodular morphology emerged with increasing deposition time. The rate of deposition thickness was 1.7–2.4 nm min<sup>-1</sup> and the loading rate was 0.8–0.9 μg cm<sup>-2</sup>·min. The deposited films were contiguous without holes. After fracturing in liquid N<sub>2</sub>, the films retained their coating integrity and did not spall from the N117 substrate. Nodular growth has been studied in detail and the resulting morphology of the film is controlled by the diffusion and/or translational velocity of the incoming particles which vary between diffusion and ballistic limits depending on the Peclet number [36,37]. Thus, a lower particle velocity and higher Pt flux will favor a more nodular and hence porous film.

Depending on the distance at which the combustion zone was quenched and the flow rate of quenching gas an amorphous or crystalline film of Pt was obtained. The diffraction patterns are plotted in Fig. 3.

These experiments suggest that the two requirements for crystalline films are a longer reaction zone, so that the clusters of atoms can coalesce and grow into nanoparticles, and a lower quench flow rate to limit the air entrainment that dilutes and hence cools the reaction zone. If the particle growth is halted, extended planar Pt(hkl) surfaces cannot form, which will have

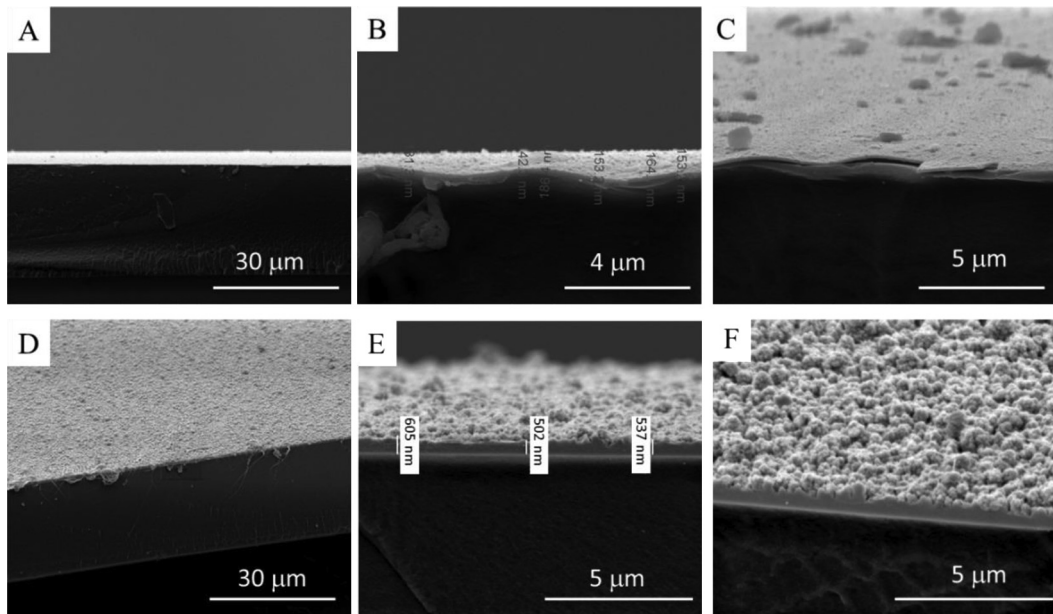


**Fig. 2.** Unsupported Pt films grown directly onto Nafion® 117 for a total deposition time of A–C) 103 min (C-Pt-103) and D–F) 230 min (D-Pt-230). Figures C and F are tilted to highlight the nodular morphology that develops with a longer deposition time.

implications on structure sensitive reactions. For instance, oxygen reduction in an acidic electrolyte is strongly structure sensitive. However, the structural sensitivity of hydrogen evolution in acid on Pt is minimal above room temperature since a compensation effect narrows the rate between the crystal faces [38]. The internal volume of non-accessible atoms must also be minimized to reduce cost, therefore an opportunity for reduction in Pt size may be possible without a loss in activity. Therefore, crystallinity should be closely monitored during scale-up and further development. Another observation is that as the location of the quench is moved further out, the loading rate increases. This result suggests that an optimization in the aerodynamics around the sample (currently an orthogonal configuration) will have profound effects on the deposition efficiency. Many of the geometries for optimizing this type of film application have been developed outside of the vapor deposition field for optical fiber-optic wave guides [39].

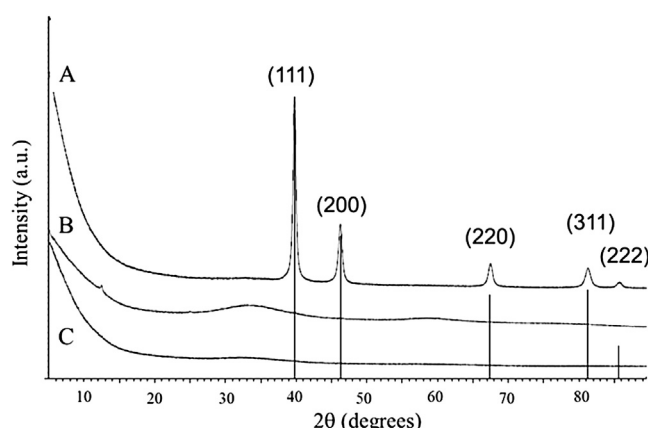


**Fig. 3.** Evolution of the Pt face-centered cubic diffraction pattern as a function of the reactive zone length (i.e., quench distance) and the volume of quench air (i.e., quench flow rate). A) 130 min (E-Pt-130); B) 110 min (F-Pt-110); C) 103 min (C-Pt-103).

### 3.3. Probing activity using rotating disk electrodes

The hydrogen evolution (Equation (1)) and oxidation (Equation (2)) activity was screened using the rotating disk electrode (RDE) technique [38,40] to explore the intrinsic surface area and kinetics of both Pt and Pt/Ebonex® films. As shown in Fig. 4A and B, the Pt surface area is greatly reduced when deposited onto the ceramic support. It is speculated that this effect may result from incomplete wetting of the electrode surface due to the presence of the ceramic support, leading to inaccuracies in the electrochemical surface area (ECA) determination [10,41]. This can occur because the Ebonex® is hydrophobic until the voltage is cycled appropriately to induce a hydrous layer on the surface [10].



HER and HOR occur on both the Pt film and the Pt/Ebonex® with similar activity as shown in Fig. 4C. The onset for HER occurs at ~0.07 V for Pt and ~0.04 V for the Pt/Ebonex®, and has a H<sub>2</sub> evolution current density of  $-25.5 \text{ mA/cm}^2_{\text{geo}}$  at -0.2 V while the Pt/Ebonex® has a H<sub>2</sub> evolution current density of  $-25.0 \text{ mA cm}^{-2}_{\text{geo}}$ . The limiting HOR current density,  $i_d$ , at 0.1 V for Pt/Ebonex® was  $2.4 \text{ mA cm}^{-2}_{\text{geo}}$  and for Pt was  $3.2 \text{ mA cm}^{-2}_{\text{geo}}$  whereas Sheng et al. found a value of  $3.1 \text{ mA cm}^{-2}$  under identical conditions [42]. The theoretical limiting current density discrepancy between the Pt and Pt/Ebonex® is likely related to the iR resistances in the Pt/Ebonex® electrode due to the excess Nafion® required for binding.

Fig. 4C also shows that Ebonex® does not exhibit any obvious redox peaks nor does there appear to be any synergistic effect of the Ebonex® with the Pt toward HER. The HOR current for both Pt and Pt/Ebonex® quickly achieves diffusional control due to the ultra-fast kinetics of the reaction. The HER does not reach diffusion control for either sample leading to a mixed kinetic and mass transport controlled current. Additionally, there was no dependence of the HER rate on the rotation rate for either Pt or Pt/Ebonex® (data not shown). The Pt film was stable after cycling the voltage for 200

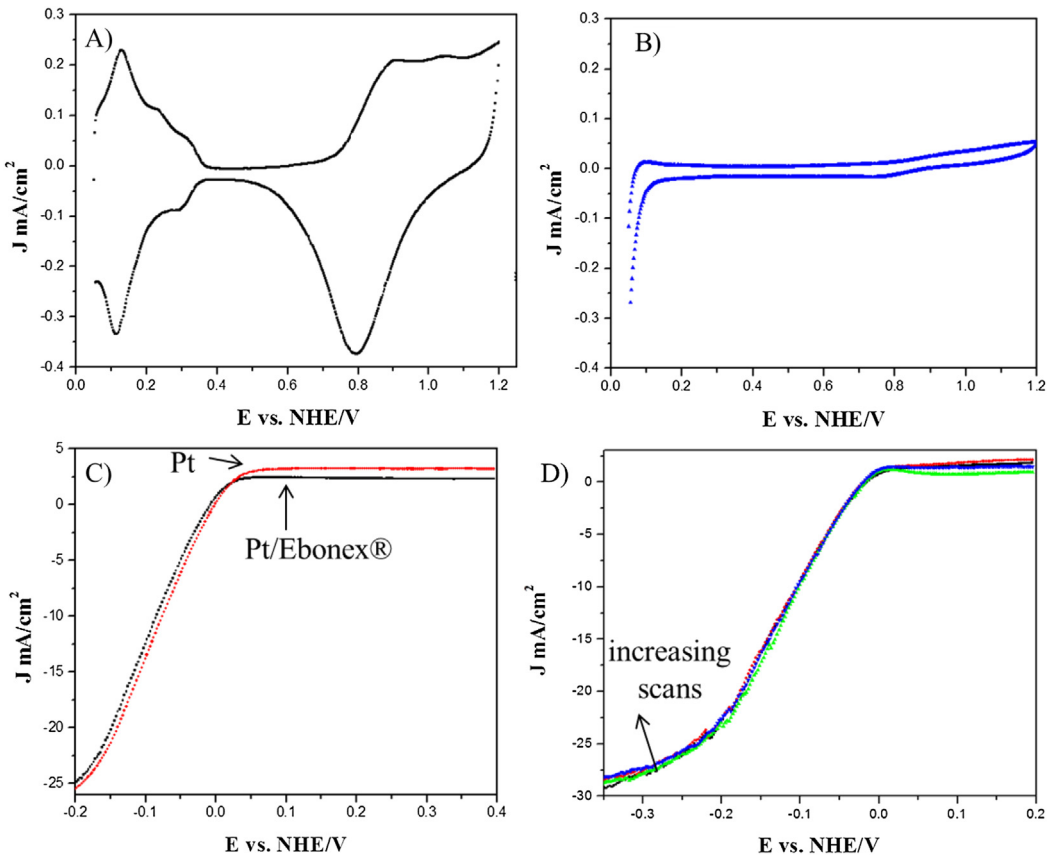


**Fig. 4.** Cyclic voltammetry of samples A-Pt-30 and B-Pt-Ebonex-30 in  $N_2$  saturated 0.1 M  $HClO_4$  to determine the electrochemically active surface area of A) a Pt film deposited directly onto the glassy carbon disk and evaluated using a scan rate of  $50\text{ mV s}^{-1}$ . The Pt loading was  $31\text{ }\mu\text{g cm}^{-2}$  leading to an electrochemical surface area of  $61\text{ m}^2\text{ g}^{-1}$ , B) Pt/Ebonex® deposited directly onto a glassy carbon disk and evaluated using a scan rate of  $20\text{ mV s}^{-1}$ . The Pt loading was  $30\text{ }\mu\text{g cm}^{-2}$  leading to an electrochemical surface area of  $5\text{ m}^2\text{ g}^{-1}$ . C) Linear sweep voltammetry in  $H_2$  saturated 0.1 M  $HClO_4$  to determine the activity of Pt and Pt/Ebonex® toward  $H_2$  evolution at potentials less than  $0.0\text{ V}$  and H oxidation at potentials  $>0.0\text{ V}$  using a rotation rate of  $1600\text{ rpm}$  and a scan rate of  $10\text{ mV s}^{-1}$ . D) Stability of the Pt film after 200 cycles between  $-0.4$  and  $0.2\text{ V}$ .

cycles as shown in Fig. 4D. At  $-0.35\text{ V}$  the current drops from  $-29.2\text{ mA cm}_{\text{geo}}^{-2}$  at cycle 1 to  $-28.2\text{ mA cm}_{\text{geo}}^{-2}$  at cycle 200, a loss of only 3.5%.

Due to the very fast reaction rates of HER and HOR, the kinetics cannot be separated from the diffusion overpotential [42]. Current densities exhibit a Nernstian hydrogen diffusion overpotential relationship and the exchange current densities (in acid) are many orders of magnitude larger than the typical hydrogen diffusion limited current density [42]. This makes accurate quantification difficult. However, these preliminary RDE studies suggest that the intrinsic activities of Pt and Pt/Ebonex® are promising and that the current densities for HER are almost double ( $25\text{ mA cm}_{\text{geo}}^{-2}$ ) of those reported elsewhere for Pt, Pt/C, and Pt/WC ( $7\text{--}12\text{ mA cm}_{\text{geo}}^{-2}$ ) at  $-0.2\text{ V}$  [43].

#### 3.4. Adhesion challenges

Upon assembly into an electrolyzer and subsequent polarization the Pt thin-film cathodes were approximately linear in voltage response up to  $2500\text{ mA cm}_{\text{geo}}^{-2}$ , as shown in Fig. 5. However, around  $1250\text{ mA cm}^{-2}$  the voltage either slightly tapers or exhibits a slight increase in slope. Upon current reversal, during the first cycle, the voltage dropped and the subsequent response was linear (Fig. 5E). On disassembly of the cell, it was observed that a majority of the catalyst on the cathode side had detached from the membrane, as shown in Fig. 5A and B.

The catalyst strips in Fig. 5A are the only remains of the deposition after disassembly of the gas diffusion layer. The micrograph

of the cathode in Fig. 5B shows very little catalyst remaining in the channels between the flow-field ribs. The adhesion of the Pt film appeared to be the most compromised, from hydrogen evolution, in areas not under direct compression of the flow field (i.e., the channels). As a mitigation strategy for the film-loss two attempts were made to fabricate Pt cathodes using a solubilized Nafion® copolymer as a binder. The Nafion® binder was  $>10\text{ wt.\%}$  in the electrode layer. Micrographs of these samples show a web-like pattern in the electrodes, assumed to be Nafion® channels (Fig. 5C and D). Imprints from the carbon fibers of the GDL are also evident in the films. The addition of the Nafion® prevented catalyst loss under the channels, however the performance was poor as seen in sample I-Pt-Nafion-118 in Fig. 5E. It is possible that the Nafion® increased the electrodes electrical resistance or reduced the accessible surface area by electrically isolating some of the Pt. Since the Pt film remained intact, this approach (with optimization) may be used on the anode side, with  $IrO_2$ , where high potentials limit acceptable catalyst support candidates.

#### 3.5. Supported Pt electrodes

Two alternative strategies were evaluated to mitigate the loss of catalyst and improve performance using a Pt support. One strategy was the addition of a porous  $Ti_{n}O_{2n-1}$  support with Nafion® (sample G-Pt-Ebonex-130). Roller et al. have previously used  $Ti_{n}O_{2n-1}$  as a support for Pt prepared by RSDT to study the oxygen reduction reaction [21]. Although no significant catalyst loss was observed in a sample with the support layer, the cell performance

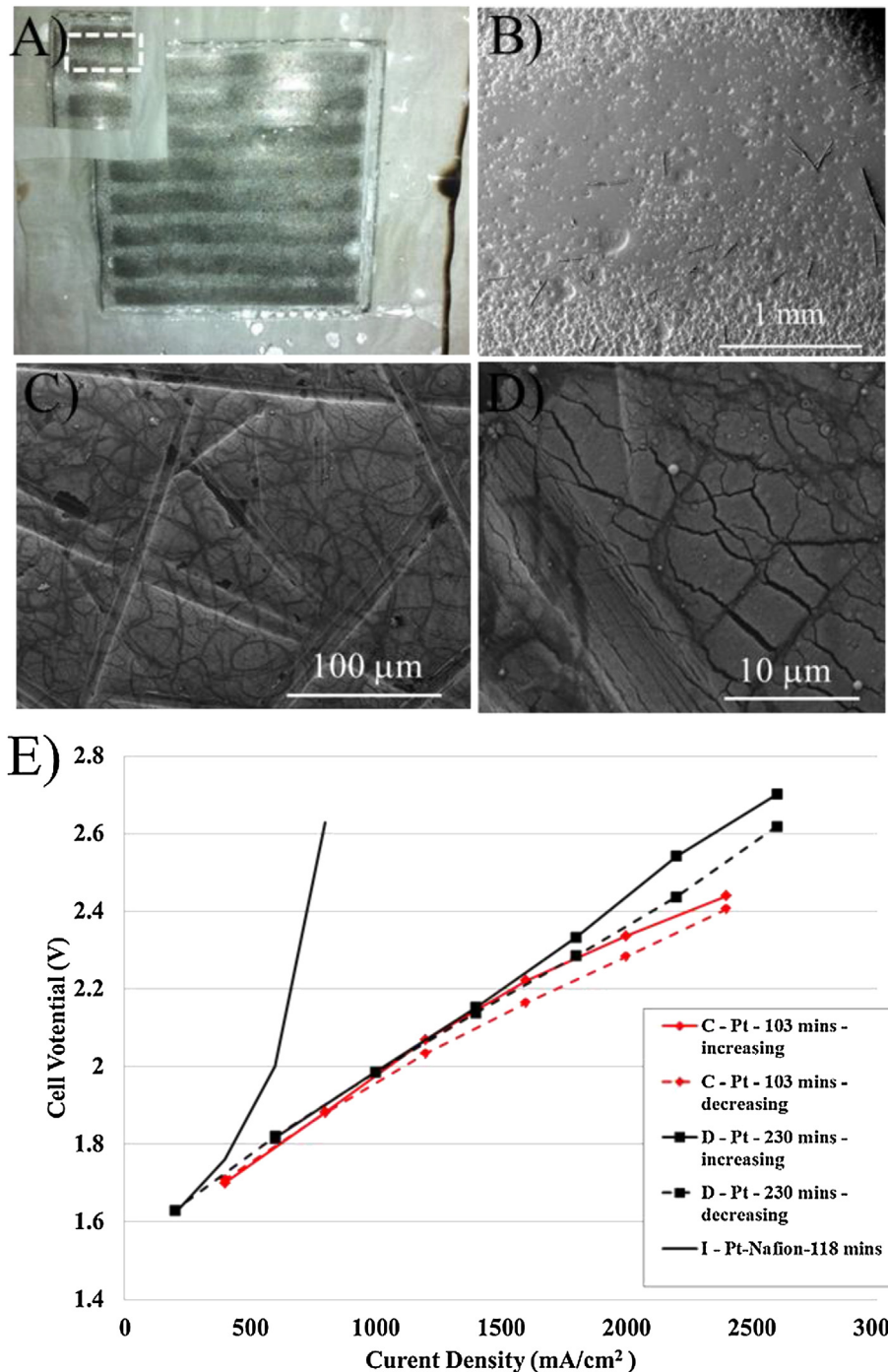


**Fig. 5.** A digital image A) and B) micrograph of sample D-Pt-230 after polarization. Catalyst loss is evident in the flow-field channels of the Pt film. C, D) Post MEA evaluation micrographs of sample I-Pt-Nafion-118 which has ionomer added as a binder. E) Plot of the cell voltage as a function of current density for samples C-Pt-103, D-Pt-230 with ( - ) increasing and ( - - ) decreasing current. Sample I-Pt-Nafion-118 is plotted for comparison and a GDL baseline ( - ) is plotted for reference.

was not improved, Fig. 6. This may be due to the reduced surface area of Pt on the ceramic support as shown in Fig. 4B. Although the results showed the addition of the  $Ti_nO_{2n-1}$  support layer on the cathode did not immediately improve performance. Further investigation of the wetting characteristics and optimizing the Nafion® content are justified.

The second strategy to improve adhesion was the addition of a carbon support with Nafion®. The Nafion® functions to bind the carbon both to itself and the substrate. In addition the Nafion® will

extend the reaction zone in the electrode by extending the triple phase boundary [44].

When Nafion® was combined with the carbon support, a sharp improvement in cell performance was observed as shown by the trends in polarization curve of the carbon supported with Nafion binder plot (H-Pt-Vulcan-227) in Fig. 6A. The new electrode formulation resulted in performance that exceeds the benchmark up to  $1000 \text{ mA cm}^{-2}$  and then deviates by  $+100 \text{ mV}$  at  $2000 \text{ mA cm}^{-2}$ .

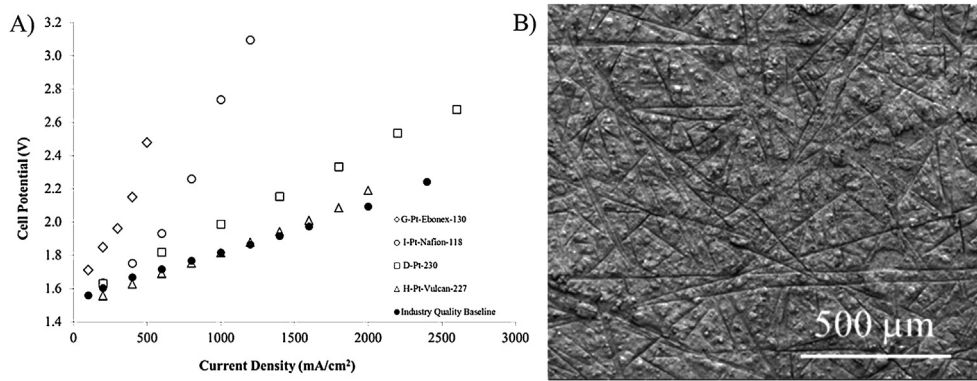


**Fig. 6.** A carbon-supported cathode with Nafion binder provides a more favorable electrode configuration than unsupported cathodes. A) Polarization data for an unsupported RSDT cathode sample D-Pt-230 (□), with Nafion binder sample I-Pt-Nafion-118 (○), and cathode supported on carbon with Nafion binder sample H-Pt-Vulcan-227 (△). A polarization scan for the cathode supported on Ebonex® with Nafion binder, G-Pt-Ebonex-130 is also plotted (◊). An industry quality baseline is plotted for reference (●). B) Sample H-Pt-Vulcan-227 post-operational micrograph of carbon-supported cathode sample with Nafion binder showing the improvement in adhesion.

Consistent with the improved cell performance, visual inspection showed catalyst still present on the electrode after disassembly with no observable distinction between the channels and ribs of the flow field. The micrograph in Fig. 6B confirms that a continuous layer of electrode material was still present on the membrane after testing. The poor performance of the Ebonex® compared to the Vulcan XC-72R support can be considered in the context of the surface area of the support determined by N<sub>2</sub> adsorption. Previous results by Roller et al. determined a Brauner–Emmett–Teller (BET) surface area of 254 m<sup>2</sup> g<sup>-1</sup> and 11.9 m<sup>2</sup> g<sup>-1</sup> respectively for Vulcan XC-72R and ball-milled Ebonex® [21]. The Nafion® functions to disperse the support in the methanol solvent prior to its role as a binder. The content of Nafion® required for binding is related to the surface area and based on this reasoning a 20× reduction in the Nafion® is necessary to bind the Ebonex®. However, as listed in Table 1 the Ebonex® sample (G-Pt-Ebonex-130) required approximately 3× the content of Nafion® to form a stable dispersion for spraying through the secondary nozzles. The amount of Nafion® per surface area is one explanation for the poor MEA performance (Fig. 6A) even though the RDE tests showed HER activity comparable to Pt (Fig. 4C).

### 3.6. Morphology of the film

All supported catalysts required the use of Nafion® 117 solution (~5wt.% in a mixture of lower aliphatic alcohols and water) as dispersant for spraying from secondary nozzles, and as a binder to ensure adhesion to the N117 substrate. Fig. 7 shows the birds-eye view and cross-sections of the supported Pt electrodes.

In addition to direct deposition onto the membrane, our substrate holder also contains tabs to concomitantly deposit the exact same film onto the TEM grids for analysis. TEM images for unsupported Pt and Pt/Ebonex are shown in Fig. 8A and B, respectively. Three distinct stages of nanoparticle growth were observed. Decomposition of the Pt-(acac)<sub>2</sub> leads to formation of a supersaturated Pt gas in the combustion zone of the turbulent jet-diffusion flame [29,45]. As the Pt gas traverses the flame field, homogeneous nucleation occurs due to the decreasing temperature. Condensation reduces the supersaturation by forming nuclei of Pt. The formation of clusters (small collections of atoms) occurs by random collision through Brownian and convective motion. The clusters dynamically form and dissociate until the partial pressure in the vicinity of the particle is larger than the vapor pressure above the curved surface [45]. Once a stable nuclei is formed, the particles continue to grow by further collisions.

Fig. 8 shows the results of STEM imaging from two areas of a TEM grid exposed to the process used to manufacture sample B-Pt-Ebonex-30 (see Table 1). Area 1 is displayed in Fig. 8A and Area 2 is shown in Fig. 8B. The TEM grid from Area 1 shows the existence of particles at different stages of growth. Arrow 1 points to a region with clusters, arrow 2 shows a ~3 nm Pt nanoparticle, and arrow 3 shows the surface agglomeration of several nanoparticles. Arrow 4 in Fig. 8B points to a 4 nm Pt particle that has attached to a ~30 nm particle of Ti<sub>n</sub>O<sub>2n-1</sub> (5). The existence of fully formed nanoparticles and small clustered associations of Pt means that particles are forming under different conditions with the smaller clusters having traversed a cooler path than the larger nanoparticles. This observation also correlates with the changes in crystallinity seen in Fig. 3. Processing conditions that favor inhomogeneous particle sizes include a low velocity for the oxidant or fuel flow jets, location of the quench (*i.e.*, in the luminous portion of the flame), and/or a quench flow rate that entrains excess air and cools the flame prematurely. A low jet velocity leads to poor mixing between the fuel and O<sub>2</sub> while a quench location extending too far into the flame will prematurely cool the forming particles to favor more clusters [46]. Finally, a high quench flow rate will entrain air behind the quench location and cool the flame [30].

Based on previous work by Roller et al. the Pt agglomerates seen in arrow 3 appear with increasing deposition time and do not form (under the conditions used in this study) in the combustion zone [10]. This same phenomena was observed during timed growth sequences of Ir<sub>x</sub>Pt<sub>1-x</sub>O<sub>2-y</sub> and Ir<sub>x</sub>Ru<sub>1-x</sub>O<sub>2-y</sub> films using RSDT [10]. Particles of Pt (such as arrow 2) randomly decorate the surface of the grid by a ballistic mechanism. After a critical density of particles exist on the grid, the additional incoming particles that cross the boundary layer are attracted to the pre-existing Pt particles, thus forming the fractal like clusters [37,47]. The number flux of Pt is higher than flux of Ebonex® particles, which explains why Pt covers more of the grid than the Ebonex® at the start of the film growth, see Fig. 8A. A thin layer of Pt forms at the N117 interface before the support material has sufficiently covered the substrate. This effect has been observed in electrode manufacture for fuel cells using RSDT and an optimal Pt thickness of ~45 nm was found [35]. The uniformity and distribution of the Pt particles is a function of the oxidant/fuel mixing ratio, the fuel flow rate, the Pt concentration, the quench distance, and the quench flow rate. Uniformity in the Pt particle size is favored by optimizing the quench conditions and using a slightly oxidizing flame.

Fig. 8C shows a representative XEDS signal from Area 2. A color-coded map of each statistically relevant component in the XEDS

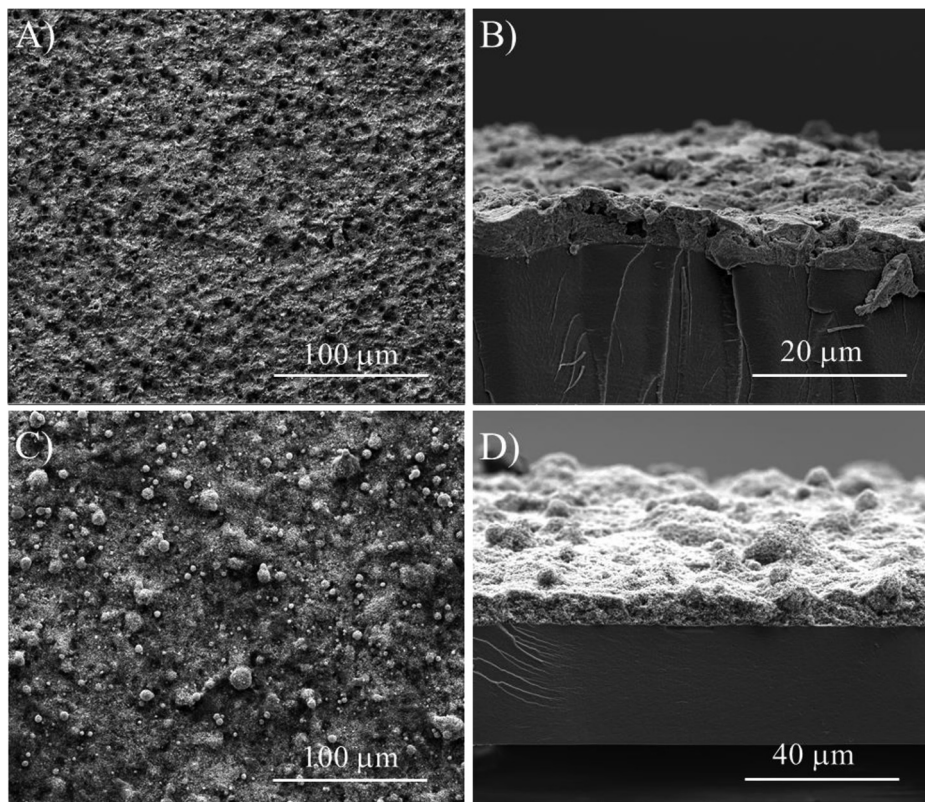


**Fig. 7.** Prior to MEA assembly, the micrographs of the RSDT deposited films in A, C) plan-view and B, D) cross-section using a support material for Pt comprising A, B) Ebonex<sup>®</sup> sample G-Pt-Ebonex-130 and, C, D) Vulcan XC-72R sample H-Pt-Vulcan-227.

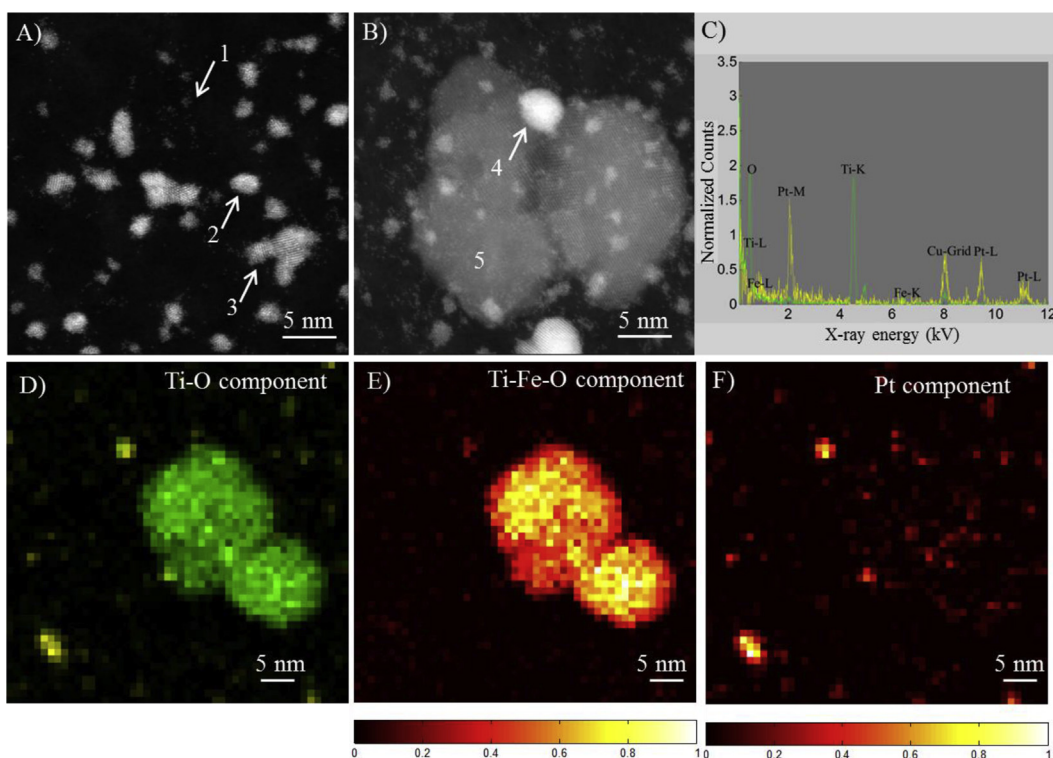


**Fig. 8.** Catalyst nanoparticles of Ebonex<sup>®</sup> and Pt deposited directly onto a Cu TEM grid. A) Pt nanoparticles and B) Pt nanoparticles decorating a larger Ebonex<sup>®</sup> support. C) XEDS map of area containing both Ebonex<sup>®</sup> and Pt particles. D) the X-ray energy dispersive spectrum of the TiO component, E) Ti–Fe–O component, and F) Pt components determined by multivariate component spectral analysis of the XEDS signals at each pixel.

signal is displayed in Fig. 8D–F. The components are determined using the multivariate analysis technique of principal component analysis [48]. The intensity of each pixel in Fig. 8D–E is related to the spectrum intensity of a principal component. For instance, the more intense color in Fig. 8E corresponds to areas where the Ti–Fe–O XEDS signal is most intense. The three components shown in Fig. 8 were determined by statistical evaluation of the XEDS plots from each pixel in the 50 × 50 pixel array (~2500 spectra). Fig. 8D shows the location of the  $Ti_nO_{2n-1}$  and Fig. 8F shows the location of the Pt. The Pt is distributed randomly on the grid and  $Ti_nO_{2n-1}$  support. Of interest is the Ti–Fe–O component. Fe is an unwanted element that is believed to have originated from the ball-milling process.

### 3.7. Durability

After finding a set of successful electrode fabrication conditions to achieve high electrochemical performance, the cathode focus shifted to durability testing. A new cathode half-MEA, using the same conditions as the electrodes in Fig. 6A to create a half MEA with Nafion® binder and a carbon support (sample J-Pt-Vulcan-224), was assembled into Proton's commercial 28 cm<sup>2</sup> hardware. Paired with a proprietary Proton anode GDE, this MEA was tested at 50 °C and 52 A (1860 mA cm<sup>-2</sup>). Data collected from this test is shown as open triangles in Fig. 9. The cell ran for 1075 h without failure before being removed. After an initial break-in period within the first few hours of operation, the sample showed impressive stability, drifting by less than 40 mV throughout the test. The increase in cell potential over the initial polarization curve data can likely be attributed to the change in cell architecture. It is suspected that the initial break-in period, which was also seen in short-term performance testing, is related to a mass transport barrier within the electrode which is reduced once electrolysis occurs for a period long enough to increase the porosity of the electrode.

In addition to testing the performance of a carbon-supported-Pt catalyst directly applied to a Nafion® substrate, an identical electrode (sample K-Pt-Vulcan-230) was fabricated directly onto Toray paper (i.e., a gas diffusion electrode, or GDE). This electrode was also assembled into Proton's commercial 28 cm<sup>2</sup> hardware and tested for durability as shown as open diamonds in Fig. 9. The performance was ~100 mV better than the sample electrode applied directly to the N117 substrate for ~600 h of operation. An initial break-in period results in a drop in voltage of ~50 mV to

~2.08 V. The voltage rises slightly over the 600 h operation to ~2.12 V (~0.07 mV h<sup>-1</sup>).

As previously discussed, the increase in carbon supported electrode performance is likely due to better distribution of catalyst on the electrode, the introduction of favorable gas pathways created by the microstructure of the carbon, and H<sup>+</sup> conducting pathways provided by the Nafion® binder. The RSDT GDE configuration operated at 70% efficiency with a 5× reduction in Pt content compared to Proton's baseline in the same format. The durability data show that efficiency can be maintained with significant catalyst reduction in production quality hardware using the RSDT deposition process.

Previous durability testing reported by Debe et al. [8], under identical conditions, using 3M's nanostructured thin-films (NSTF) of PtCoMn and PtIr with loadings of 0.15 mg<sub>PGM</sub> cm<sup>-2</sup> showed a stable voltage of ~1.95 V at 1860 mA cm<sup>-2</sup> over 3000 h. Results from Debe et al. were the outcome of over two dozen tests over a three-year period. With further RSDT process development and optimization of both GDL and membrane depositions a reduction of 50–65 mV is probable.

## 4. Conclusions

A deposition study using RSDT to apply Pt, Pt/Nafion®, Pt/Ebonex®, and Pt/Vulcan XC-72R onto N117 and Toray paper was completed. Bubble formation during H<sub>2</sub> evolution warrants the use of a binder to hold the catalyst to the substrate. The amount of binder needed to disperse the Ebonex® may cover the Pt catalyst and therefore more work must be done to determine alternate routes for dispersion. This work suggests that matching the binder content to the BET determined surface area would be an appropriate approach for further electrode optimization. All combinations of catalyst with Nafion® as the binder remained intact after polarization. However, only the carbon support had sufficient surface area (254 m<sup>2</sup> g<sup>-1</sup> versus 11.9 m<sup>2</sup> g<sup>-1</sup> for ball-milled Ebonex®) to incorporate the Nafion® from the slurry into the electrode as suggested by the very large ohmic resistances seen during polarization. Deposition of the Pt/Vulcan XC-72R onto Toray paper resulted in the best performance. Future work should examine optimization of process parameters onto the Toray paper and incorporation of a microporous layer.

## References

- [1] The Impact of Increased Use of Hydrogen on Petroleum Consumption and Carbon Dioxide Emissions, US Energy Information Administration (EIA), 2008. SR-OIAF-CNEAF/2008-04.
- [2] J. Genovese, K. Harg, M. Paster, J. Turner, Current (2009) State-of-the-Art Hydrogen Production Cost Estimate Using Water Electrolysis, 2009. NREL/BK-6A1–46676.
- [3] Water Electrolysis and Renewable Energy Systems, Fuel Cell Today, 2013.
- [4] E. Rasten, G. Hagen, R. Tunold, *Electrochim. Acta* 48 (2003) 3945–3952.
- [5] S.A. Grigoriev, P. Millet, V.N. Fateev, *J. Power Sources* 177 (2008) 281–285.
- [6] E. Slavcheva, I. Radev, S. Bliznakov, G. Topalov, P. Andreev, E. Budevski, *Electrochim. Acta* 52 (2007) 3889–3894.
- [7] M.K. Debe, S.M. Hendricks, G.D. Vernstrom, M. Meyers, M. Brostrom, M. Stephens, et al., *J. Electrochem. Soc.* 159 (2012) K165–K176.
- [8] J. Roller, K.E. Ayers, W.E. Mustain, R. Maric, Hydrogen Evolution on Combustion Catalyzed Electrodes with Low Loadings for PEM Electrolyzers, in: ECS 223rd Meeting Toronto May 12–17th, 2013.
- [9] J.M. Roller, M. Josefina Arellano-Jiménez, R. Jain, H. Yu, C. Barry Carter, R. Maric, *J. Electrochem. Soc.* 160 (2013) F716–F730.
- [10] J.M. Roller, J. Arellano-Jiménez, R. Jain, R. Maric, B. Carter, Activity and Microstructure of Oxygen Evolution Anodes Prepared by a Direct Dry Deposition Technique, Meeting Abstracts MA2012-01, 2012, pp. 97–106.
- [11] W.Y. Teoh, R. Amal, L. Madler, *Nanoscale* 2 (2010) 1324–1347.
- [12] G.L. Messing, S. Zhang, G.V. Jayanthi, *J. Am. Ceram. Soc.* 76 (1993) 2707–2726.
- [13] J. Roller, R. Neagu, F. Orfino, R. Maric, *J. Mater. Sci.* 47 (2012) 4604–4611.
- [14] R. Maric, J. Roller, R. Neagu, *J. Therm. Spray. Technol.* 20 (2011) 696.
- [15] R. Maric, R. Neagu, Y. Zhang-Steenwinkel, F.P.F. van Berk, B. Rietveld, *J. Power Sources* 195 (2010) 8198–8201.

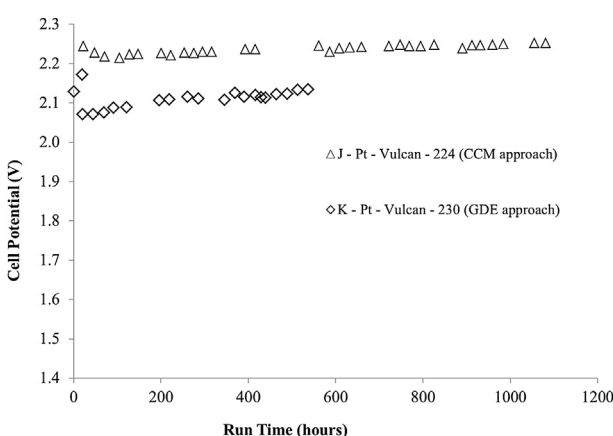


Fig. 9. Durability test data for RSDT manufactured cathodes deposited on Nafion® by the CCM route J-Pt-Vulcan-224 (△) and on Toray paper using the GDE route K-Pt-Vulcan-230 (◊).

- [17] R. Nédélec, R. Neagu, S. Uhlenbruck, R. Maric, D. Sebold, H.- Buchkremer, et al., *Surf. Coat. Technol.* 205 (2011) 3999–4004.
- [18] K. Fatih, R. Neagu, V. Alazate, V. Neburchilov, R. Maric, W. Haijiang, *ECS Trans.* 25 (2009) 1177–1183.
- [19] R. Maric, J.M. Roller, R. Neagu, K. Fatih, A. Tuck, *ECS Trans.* 12 (2008) 59–63.
- [20] R. Maric, in: J. Zhang (Ed.), *PEM Fuel Cell Electrocatalysts and Catalyst Layers: Fundamentals and Applications*, vol. 1, Springer, 2008.
- [21] J.M. Roller, M.J. Arellano-Jiménez, H. Yu, R. Jain, C.B. Carter, R. Maric, *Electrochim. Acta* 107 (2013) 632–655.
- [22] A. Camenzind, W.R. Caseri, S.E. Pratsinis, *Nano Today* 5 (2010) 48–65.
- [23] G.D. Ulrich, *Chem. Eng. News* 62 (1984) 22–29.
- [24] S.E. Pratsinis, *Prog. Energy Combust. Sci.* 24 (1998) 197–219.
- [25] P. Roth, *Proc. Combust. Inst.* 31 (2007) 1773–1788.
- [26] M.S. Wooldridge, *Prog. Energy Combust. Sci.* 24 (1998) 63–87.
- [27] M.C. Heine, L. Mädler, R. Jossen, S.E. Pratsinis, *Combust. Flame* 144 (2006) 809–820.
- [28] W.R. Hawthorne, D.S. Weddell, H.C. Hottel, *Symposium Combust. Flame Explos. Phenom.* 3 (1949) 266–288.
- [29] H.K. Kammler, L. Mädler, S.E. Pratsinis, *Chem. Eng. Technol.* 24 (2001) 583–596.
- [30] K. Wegner, S.E. Pratsinis, *AIChE J.* 49 (2003) 1667–1675.
- [31] K.A. Mauritz, R.B. Moore, *Chem. Rev.* 104 (2004) 4535–4586.
- [32] S. Flanagan, E. Hall, W. Bowie, J.W. Fuhs, R. Logan, F. Maniei, et al., *Green Chem.* 7 (2005) 333–338.
- [33] M. Womes, T. Cholley, F.L. Peltier, S. Morin, B. Didillon, N. Szydlowski-Schildknecht, *Appl. Catal. A* 283 (2005) 9–22.
- [34] H.M.N.H. Irving, J.S. Smith, S. Karmali, J. Inorg. Nucl. Chem. 43 (1981) 1139–1140.
- [35] J. Roller, *Low Platinum Electrodes for Proton Exchange Fuel Cells Manufactured by Reactive Spray Deposition Technology*, 2009.
- [36] L. Mädler, A. Roessler, S.E. Pratsinis, T. Sahm, A. Gurlo, N. Barsan, et al., *Sens. Actuators B Chem.* 114 (2006) 283–295.
- [37] L. Mädler, S. Friedlander, *Aerosol Air Qual. Res.* 7 (3) (2007) 304–342.
- [38] N.M. Marković, B.N. Grgur, P.N. Ross, *J. Phys. Chem. B* 101 (1997) 5405–5413.
- [39] G.M. Graham, M.K. Alam, *Aerosol Sci. Technol.* 15 (1991) 69–76.
- [40] H.A. Gasteiger, N.M. Markovic, P.N. Ross, *J. Phys. Chem.* 99 (1995) 8290–8301.
- [41] D. Kuscer, J. Kováč, M. Kosec, R. Andriesen, *J. Eur. Ceram. Soc.* 28 (2008) 577–584.
- [42] W. Sheng, H.A. Gasteiger, Y. Shao-Horn, *J. Electrochem. Soc.* 157 (2010) B1529–B1536.
- [43] Y. Liu, W.E. Mustain, *Int. J. Hydrogen Energy* 37 (2012) 8929–8938.
- [44] W. Xu, K. Scott, *Int. J. Hydrogen Energy* 35 (2010) 12029–12037.
- [45] T. Kodas, M. Hampden-Smith, *Aerosol Processing of Materials*, Wiley-VCH, New York, 1999.
- [46] I. Glassman, *Combustion*, Academic Press, Inc., New York, 1977.
- [47] Lutz Mädler, Anshuman A. Lall, Sheldon K. Friedlander, *Nanotechnology* 17 (2006) 4783.
- [48] P.G. Kotula, M.R. Keenan, *Microsc. Microanal.* 12 (2006) 538–544.